GEOPHYSICS, VOL. 91, NO. 1 (JANUARY-FEBRUARY 2026); P. WA23–WA33, 9 FIGS., 1 TABLE.
10.1190/GEO2025-0034.1

Two-temperature thermoporoelastic modeling in sandstone reservoirs for CO_2 sequestration monitoring

Wanting Hou[1], Li-Yun Fu[2], José M. Carcione[3], and Boris Gurevich[4]

ABSTRACT

Effective geologic carbon sequestration depends on a thorough understanding of the thermomechanical behavior of CO_2 and water in subsurface environments. This study introduces a two-temperature thermoporoelastic model that effectively captures the temperature gradient between the solid matrix and pore fluid, which is critical for addressing key challenges in CO_2 storage monitoring. By combining previous experimental measurements with numerical simulations, we investigate how temperature-dependent fluid properties, fluid type, and saturation influence seismic wave propagation in sandstone. The results reveal pronounced variations in seismic velocity and attenuation between water- and CO_2-saturated conditions, highlighting the significant role of fluid properties in reservoir behavior and seismic response. Importantly, model predictions agree well with available experimental data, demonstrating its potential for enhancing the accuracy of real-time CO_2 storage monitoring.

INTRODUCTION

Growing concern about climate change has led to a global need to reduce greenhouse gas emissions (Dowell et al., 2010). Carbon capture and storage (CCS) is a key technology to reduce atmospheric CO_2 concentrations, with CO_2 geologic sequestration (CGS) being a crucial solution to achieve carbon neutrality (Aminu et al., 2017; Lin et al., 2024). CGS, especially in deep underground formations such as saline aquifers, depleted oil and gas fields, and unmineable coal seams, has proven to be one of the most feasible methods for large-scale CO_2 sequestration (Shi and Durucan, 2005; Kalam et al., 2021; Fentaw et al., 2024; Lin et al., 2024). Among the various rock types, sandstone reservoirs are particularly suitable due to their high porosity and permeability, which enable efficient fluid flow and provide significant storage capacity (Shi et al., 2007; Otu et al., 2023).

The successful implementation of CCS relies on a thorough understanding of CO_2 behavior within geologic formations. The thermodynamics of CO_2 and reservoir fluids, before and after injection, are crucial for the effectiveness of storage efforts. This is especially true for the effects of temperature on the pore architecture and elastic properties of reservoir rocks (Xue and Lei, 2006; Lebedev et al., 2014; Zhang et al., 2024). Temperature plays a significant role in determining the physical state and thermal properties of CO_2 and reservoir fluids, influencing migration, trapping efficiency, and long-term stability in the subsurface (Awad and Espinoza, 2024; Creasy et al., 2024; Zhang et al., 2024). When CO_2 is injected into sandstone reservoirs in its supercritical state ($scCO_2$), it exhibits distinct thermodynamic properties (such as viscosity, density, and thermal conductivity) that are highly temperature dependent (Liao et al., 2023). Therefore, understanding the impact of temperature on CO_2 behavior and reservoir fluids is essential for optimizing CO_2 sequestration strategies and ensuring the safety and effectiveness of CGS.

The poroelasticity theory of Biot (1956) serves as the basis for studying wave propagation in fluid-saturated porous media. However, its application to CGS mechanisms and monitoring has been limited, primarily due to the neglect of temperature effects. To address this, the theory of thermoelasticity, which couples displacement and temperature fields (Biot, 1962), has been further developed with models such as the Lord-Shulman (LS) model (Lord and Shulman, 1967), which incorporates a single relaxation time,

Manuscript received by the Editor 23 January 2025; revised manuscript received 23 April 2025; published ahead of production 12 June 2025; published online 21 August 2025.
[1]Chengdu University of Technology, College of Geophysics, Chengdu, China; China University of Petroleum (East China), State Key Laboratory of Deep Oil and Gas, Qingdao, China; and Qingdao Marine Science and Technology Center, Laboratory for Marine Mineral Resources, Qingdao, China. E-mail: houwt@cdut.edu.cn.
[2]China University of Petroleum (East China), State Key Laboratory of Deep Oil and Gas, Qingdao, China and Qingdao Marine Science and Technology Center, Laboratory for Marine Mineral Resources, Qingdao, China. E-mail: lfu@upc.edu.cn (corresponding author).
[3]National Institute of Oceanography and Applied Geophysics — INOGS, Trieste, Italy. E-mail: jose.carcione@gmail.com.
[4]Curtin University, Centre for Exploration Geophysics, School of Earth and Planetary Sciences, Western Australia, Australia. E-mail: b.gurevich@curtin.edu.au.

and the Green-Lindsay (GL) model (Green and Lindsay, 1972), which accounts for two relaxation times. These models have provided a theoretical framework for seismic wave propagation in high-temperature reservoirs (Carcione et al., 2018; Hou et al., 2021, 2023).

More recently, heat conduction equations have been integrated with Biot's poroelasticity to better capture the complexity of real rock, leading to the development of the theory of thermoporoelasticity (Noda, 1990; Carcione et al., 2019). Zimmerman (2000) notes that although temperature fields can influence stresses and strains, the reverse effect is minimal. However, thermal effects significantly impact P-wave characteristics in inhomogeneous media, particularly causing increased attenuation and velocity dispersion. Xi et al. (2007) find that the attenuation peaks in saturated rocks exhibit typical thermally activated relaxation behavior, indicating that thermal effects significantly influence P-wave attenuation and dispersion. Xi et al. (2011) further develop a model based on thermal activation mechanisms, revealing the impact of thermal effects on P-wave propagation characteristics in the frequency and temperature domains, particularly in heterogeneous media. Wei et al. (2020, 2022, 2023) also demonstrate that thermal effects significantly influence P-wave scattering attenuation and velocity dispersion in nonuniform media, such as those with fractures and nonisothermal inclusions. The study by Wang et al. (2022) emphasizes the complexity of thermoelastic attenuation in randomly distributed layered media, further confirming the significant impact of thermal effects on P-wave characteristics in heterogeneous media.

Li et al. (2023, 2024) extend the LS thermoporoelasticity model to account for double porosity and incorporate local heat flow and local fluid flow. These factors are crucial for evaluating the seismic properties of geothermal reservoirs and understanding the effects of temperature, pore structure, and pore fluid on thermoelastic properties during cyclic recovery processes. In addition, Deng et al. (2024) refine a double porosity model by introducing nonlinear viscosity, which improves the understanding of the macroscopic mechanical behavior of fluid-saturated sandstone at different temperatures. Liu et al. (2023) use finite-difference algorithms to study wave propagation within the dual-phase lag (DPL) heat conduction model of Tzou (1995). However, the preceding models are based on the assumption of a single temperature (ST-LS, ST-GL and ST-DPL), which ignores the temperature gradient between the solid skeleton and the pore fluid. To address this limitation, Youssef (2007) proposes a two-temperature generalized (TTG) equation to account for this difference, a concept that was subsequently explored by Singh (2011). Based on the TTG-LS and TTG-GL theories, Hou et al. (2024) develop a fluid-saturated thermoporoelastic amplitude-variation-with-offset model that provides new insights into the behavior of CO_2 in geologic reservoirs. This model represents a significant advance in the understanding and simulation of thermoelastic effects in CGS.

This study examines the thermal-mechanical behavior of CO_2 and water in underground environments, a critical factor for ensuring the effectiveness and safety of CGS. The research begins by examining the temperature dependence of fluid thermoelastic parameters (density, specific heat, viscosity, coefficient of thermal expansion, thermal conductivity, and bulk modulus) using data from the reference fluid thermodynamic and transport properties (REFPROP) database (Lemmon et al., 2013). Subsequently, the propagation and attenuation characteristics of seismic waves in water- and $scCO_2$-saturated sandstone are analyzed based on the two-temperature model. The predicted seismic wave velocities show agreement with experimental data, demonstrating the model efficacy in monitoring CO_2 storage. By combining experimental measurements with numerical simulations, this study investigates how fluid type, saturation, and temperature affect seismic wave propagation, highlighting the critical role of fluid properties in seismic response and reservoir behavior.

TTG THERMOPOROELASTIC THEORY

According to Youssef (2007), the generalized thermoporoelastic medium takes into account the temperature difference between the fluid and the solid skeleton, assuming that the fluid can exert a velocity-dependent frictional force on the solid, whereas the viscous stresses in the fluid are neglected. The two phases have different temperatures, so that an energy exchange occurs during wave propagation. The model is homogeneous and isotropic, with a compressible and ideal fluid filling where both phases are continuous and interact with each other, leading to thermomechanical coupling.

The fundamental governing equation for the TTG model couples mechanical deformation, fluid flow, and heat conduction, considering the temperature difference between the solid skeleton and pore fluid. Specifically, the displacement vectors of the frame and fluid relative to the frame are denoted by $\mathbf{u} = (u_x, u_y, u_z)$ and $\mathbf{w} = (w_x, w_y, w_z)$, respectively, with T_s and T_f being the temperature of the solid and the fluid relative to respective reference temperatures T_0^s and T_0^f. The governing equation is expressed as

$$\bar{\boldsymbol{\mu}}\nabla^2\bar{\mathbf{U}} + \bar{\mathbf{K}}\,\bar{\nabla}\,\bar{\boldsymbol{\epsilon}} + \boldsymbol{\Xi} = \bar{\boldsymbol{\rho}}\,\bar{\mathbf{W}}, \tag{1}$$

where matrices $\bar{\mathbf{K}}$, $\bar{\rho}$, and $\bar{\mu}$ represent the thermal and elastic constants and vectors $\bar{\mathbf{U}}$, $\bar{\epsilon}$, Ξ, and $\bar{\mathbf{W}}$ represent the displacement fields, strain components, and temperature fields of solid and fluid phases, respectively. Here, ∇^2 is the Laplacian operator and

$$\begin{aligned}
\bar{\mathbf{U}} &= [\,\mathbf{u} \quad \mathbf{w} \quad T_s \quad T_f\,]^{\top},\\
\bar{\boldsymbol{\epsilon}} &= [\,\epsilon_m \quad \epsilon_f \quad T_s \quad T_f\,]^{\top},\\
\bar{\mathbf{W}} &= [\,\ddot{\mathbf{u}} \quad \ddot{\mathbf{w}} \quad \dot{\mathbf{w}}\,]^{\top},\\
\boldsymbol{\Xi} &= [\,0 \quad 0 \quad \bar{\gamma}_{sf}(T_s - T_f) \quad -\bar{\gamma}_{sf}(T_s - T_f)\,]^{\top},
\end{aligned} \tag{2}$$

and

$$\bar{\boldsymbol{\mu}} = \begin{bmatrix} \mu & 0 & 0 & 0\\ 0 & 0 & 0 & 0\\ 0 & 0 & -\bar{\gamma}_s & 0\\ 0 & 0 & 0 & -\bar{\gamma}_f \end{bmatrix}, \quad \bar{\nabla}_{\iota j} = \begin{cases} \nabla, & \iota = 1 \text{ or } 2\\ \wedge_{2s}^2, & \iota = 3\\ \wedge_{2f}^2, & \iota = 4 \end{cases}, \tag{3}$$

where $\bar{\gamma}$ is the thermal conductivity (subscripts "s" and "f" denote the solid and fluid, respectively), μ is a Lamé constant,

$$\bar{\mathbf{K}} = \begin{bmatrix} E_G & \bar{\alpha}M & -R_{11}\wedge_{1s} & -R_{12}\wedge_{1f}\\ \bar{\alpha}M & M & -R_{21}\wedge_{1s} & -R_{22}\wedge_{1f}\\ T_0^s R_{11} & T_0^f R_{21} & F_{11} & F_{12}\\ T_0^s R_{12} & T_0^f R_{22} & F_{21} & F_{22} \end{bmatrix}, \quad \bar{\boldsymbol{\rho}} = \begin{bmatrix} \rho & \rho_f & 0\\ \rho_f & m & b\\ 0 & 0 & 0\\ 0 & 0 & 0 \end{bmatrix}, \tag{4}$$

and $\rho = (1-\bar{\phi})\rho_s + \bar{\phi}\rho_f$ is the bulk density depending on the porosity $\bar{\phi}$ and the solid and fluid densities ρ_s and ρ_f. Moreover,

$$m = \mathcal{T}\rho_f/\bar{\phi}, \quad b = \eta/\bar{\kappa}, \tag{5}$$

where $\mathcal{T}$ is the tortuosity, η is the fluid viscosity, and $\bar{\kappa}$ is the frame permeability. For improving clarity, detailed definitions and physical interpretations of parameters used in these equations are provided in Appendix A.

PLANE-WAVE ANALYSIS FOR THE TTG MODEL

To analyze wave propagation characteristics under the TTG model, we apply the Helmholtz decomposition (Wang et al., 2021). The governing equation (equation 1) can thus be reformulated in terms of compressional and shear potentials:

$$\bar{\boldsymbol{\mu}}^*\nabla^2\bar{\mathbf{U}} + \bar{\mathbf{K}}^*\bar{\nabla}^*\bar{\boldsymbol{\Phi}} = \bar{\boldsymbol{\rho}}\bar{\boldsymbol{\Phi}}^*, \quad \bar{\bar{\boldsymbol{\mu}}}\nabla^2\bar{\boldsymbol{\Psi}} = \bar{\boldsymbol{\rho}}^*\bar{\boldsymbol{\Psi}}^*, \tag{6}$$

which separates the compressional and shear components and clarifies the structure of the wave equations used for numerical simulation. Here, the matrices $\bar{\boldsymbol{\mu}}^*$, $\bar{\mathbf{K}}^*$, and $\bar{\nabla}^*$ retain the same structure as $\bar{\boldsymbol{\mu}}$, $\bar{\mathbf{K}}$, and $\bar{\nabla}$ introduced previously (equations 3 and 4), except

$$\begin{aligned} &\bar{\mu}^*(1,1) = 0, \\ &\bar{K}^*(1,1) = \bar{K}(1,1) + \mu, \\ &\bar{\nabla}^*(i,j) = \nabla^2, \quad i = 1 \text{ or } 2 \end{aligned} \tag{7}$$

and

$$\begin{aligned} &\bar{\boldsymbol{\Phi}} = [\phi_s \quad \phi_f \quad T_s \quad T_f]^\top, \quad \bar{\boldsymbol{\Phi}}^* = [\ddot{\phi}_s \quad \ddot{\phi}_f \quad \dot{\phi}_f]^\top, \\ &\bar{\boldsymbol{\Psi}} = [\psi_s \quad \psi_f]^\top, \quad \bar{\boldsymbol{\Psi}}^* = [\ddot{\psi}_s \quad \ddot{\psi}_f \quad \dot{\psi}_f]^\top, \\ &\bar{\bar{\boldsymbol{\mu}}} = [\mu \quad 0], \qquad \bar{\boldsymbol{\rho}} = \begin{bmatrix} \rho & \rho_f & 0 \\ \rho_f & m & b \end{bmatrix}. \end{aligned} \tag{8}$$

We use the general forms of potential functions and the corresponding wave amplitudes for numerical simulations of seismic wave propagation:

$$\bar{\boldsymbol{\Phi}} = \mathbf{A}_\mathrm{P}\exp[\mathrm{i}(\mathbf{k}_\mathbf{P}\cdot\mathbf{x} - \omega t)], \ \bar{\boldsymbol{\Psi}} = \mathbf{A}_\mathrm{S}\exp[\mathrm{i}(\mathbf{k}_\mathbf{S}\cdot\mathbf{x} - \omega t)], \tag{9}$$

where ω is the frequency, $\mathbf{k}$ is the wavenumber, $\mathbf{x}$ is the spatial vector,

$$\mathbf{A}_\mathrm{P} = [A_s^\mathrm{P} \quad A_f^\mathrm{P} \quad A_{Ts}^\mathrm{P} \quad A_{Tf}^\mathrm{P}]^\top, \quad \mathbf{A}_\mathrm{S} = [A_s^\mathrm{S} \quad A_f^\mathrm{S}]^\top, \tag{10}$$

where A^P and A^S are the amplitudes of the P and S waves, respectively.

By substituting the potential functions (equation 9) into the TTG system of P waves (equation 6), we obtain the dispersion relation to investigate the frequency-dependent behavior of seismic velocities:

$$B_8 \cdot k_\mathrm{P}^8 + B_6 \cdot k_\mathrm{P}^6 + B_4 \cdot k_\mathrm{P}^4 + B_2 \cdot k_\mathrm{P}^2 + B_0 = 0, \tag{11}$$

where coefficients B are given in Appendix B. The analytical solution yields four longitudinal wave modes, listed by decreasing phase velocity: P1, P2, T1, and T2 waves, which reflect the multiphysics nature of wave propagation in thermo-hydro-mechanically coupled porous media.

In contrast, a similar wavenumber relation of the S wave is (Hou et al., 2024)

$$k_\mathrm{S}^2 = \omega^2\left[\frac{\rho}{\mu} - \frac{\omega\rho_f^2}{\mu(\omega m + \mathrm{i}b)}\right]. \tag{12}$$

The phase velocity V_ph and attenuation coefficient L are (Hou et al., 2024)

$$\mathbf{V}_\mathrm{ph} = \frac{\omega}{\kappa}\hat{\boldsymbol{\kappa}}, \quad L = 4\pi\frac{A\cdot V_\mathrm{ph}}{\omega}, \tag{13}$$

where the dispersion equations are directly applied to demonstrate the relationship between frequencies and velocities (or attenuation coefficients) and

$$\mathbf{k} = \boldsymbol{\kappa} + \mathrm{i}\boldsymbol{\alpha} = \kappa\hat{\boldsymbol{\kappa}} + \mathrm{i}\alpha\hat{\boldsymbol{\alpha}}, \tag{14}$$

where $\boldsymbol{\alpha}$ is the attenuation vector and the overhat defines a unit vector.

Here, V_ph and L calculated from the complex wavenumber k (equations 11 and 12) provide critical parameters for interpreting seismic wave data in CO_2 sequestration monitoring. Specifically, these parameters enable the quantitative evaluation of seismic responses under varying reservoir conditions.

THERMOPOROELASTIC PROPERTIES OF CO_2 AND WATER

Understanding the thermomechanical behavior of water and CO_2 under different temperature and pressure conditions is essential for CGS. The thermoporoelastic properties of fluids play a key role in determining their behavior within the subsurface environment and in influencing the overall performance of CO_2 storage sites. These properties also are critical for predicting the behavior of injected CO_2, including the injectivity, migration, and longterm containment of CO_2 within geologic formations. This section provides a comprehensive characterization of the temperature- and pressure-dependent properties of CO_2 and water, based on the REFPROP database (Lemmon et al., 2013).

The effects of temperature and pressure on the density, specific heat, viscosity, thermal expansion coefficient, thermal conductivity, and bulk modulus of CO_2 are shown in Figure 1a–1f, respectively. As CO_2 transitions into the supercritical state, its density is significantly influenced by temperature and pressure, as shown in Figure 1a. At constant pressure, an increase in temperature results in a decrease in density due to the thermal expansion of CO_2 molecules. This behavior is attributed to the increased average kinetic energy of the molecules at higher temperatures, which causes the molecules to move further apart. In contrast, at constant temperature, an increase in pressure leads to an increase in density, reflecting the compressibility of $scCO_2$. For example, at 12 MPa, the density of $scCO_2$ starts at approximately 1200 kg/m^3 at 230 K and decreases to approximately 300 kg/m^3 at 370 K, representing a 75% reduction, where $T(°C) = T(K) - 273.15$. This decrease is less pronounced at higher pressures, such as 42 MPa, where the density change over the same temperature range is only approximately 33%. Beyond the critical point (304.1 K,

7.38 MPa) (Parisio and Vilarrasa, 2020), the sensitivity of $scCO_2$ density to temperature diminishes, which is characteristic of supercritical fluids. In the supercritical region, the specific heat remains relatively constant but shows a slight increase with increasing temperature, as shown in Figure 1b. This behavior is typical of supercritical fluids, which exhibit reduced sensitivity to temperature changes. At 230 K and 32 MPa, the specific heat is approximately 1.8 $kJ/(kg \cdot K)$, and it increases to approximately 2 $kJ/(kg \cdot K)$ at 370 K, representing an 11% increase.

The specific heat of CO_2 in the supercritical state is higher than in the subcritical state, a difference attributed to increased molecular interactions and the coexistence of liquid- and gas-like properties. The $scCO_2$ exhibits liquid-like density and gas-like viscosity, resulting in unique thermal properties that distinguish it from liquid and gas. As shown in Figure 1c, the viscosity decreases with increasing temperature due to the higher kinetic energy of the molecules at elevated temperatures, which reduces intermolecular forces and consequently the viscosity. At higher pressures, the viscosity increases due to increased density and enhanced molecular interactions. For instance, at 220 K and 32 MPa, the viscosity of CO_2 is approximately 2.7×10^{-4} Pa · s, and it decreases to approximately 0.7×10^{-4} Pa · s at 380 K, which is a 74% reduction. The thermal expansion coefficient, shown in Figure 1d, quantifies the fractional change in volume per unit temperature change. This coefficient increases with temperature, indicating that $scCO_2$ becomes more sensitive to temperature variations. Specifically, at 230 K, the coefficient is approximately $0.0025K^{-1}$, rising to approximately 0.006 K^{-1} at 370 K, a significant increase. Figure 1e shows the thermal conductivity of $scCO_2$, which behaves differently from typical gases. It decreases with increasing temperature because the reduced effectiveness of energy transfer occurs when molecules move further apart. At 230 K, the thermal conductivity is approximately 0.19 $W/(m \cdot K)$, decreasing to approximately 0.09 $W/(m \cdot K)$ at 370 K. Although pressure has a less pronounced effect on thermal conductivity than temperature, an increase in pressure results in a higher density, which leads to more frequent molecular collisions and, consequently, higher thermal conductivity. Figure 1f shows the bulk modulus, a critical parameter for assessing the mechanical behavior of CO_2, particularly in geologic carbon sequestration. The bulk modulus increases with pressure, indicating that CO_2 becomes more incompressible under higher pressures. It also is more sensitive to temperature, with an 87% increase at 230 K compared with 370 K under 32 MPa.

The properties of water, as depicted in Figure 2, show distinct differences from those of $scCO_2$ as functions of temperature and pressure. The density of water increases with pressure but decreases with temperature, exhibiting a 0.02% reduction from 280 to 350 K, which is less sensitive compared with the behavior of $scCO_2$, as shown in Figures 1a and 2a. In Figure 2b, the specific heat of water remains relatively constant at approximately 4.1 $kJ/(kg \cdot K)$, which is higher than that of $scCO_2$ under similar conditions, emphasizing water's superior heat retention capacity. Water's viscosity and thermal expansion coefficient, as shown in Figure 2c and 2d, are more significantly influenced by temperature than by pressure. In contrast to the negative correlation observed between temperature and thermal conductivity in $scCO_2$, water exhibits a positive correlation. This difference can be attributed to the increased molecular collisions and energy transfer in water as temperature rises, whereas in $scCO_2$, molecules move further apart and intermolecular interactions weaken due to the unique

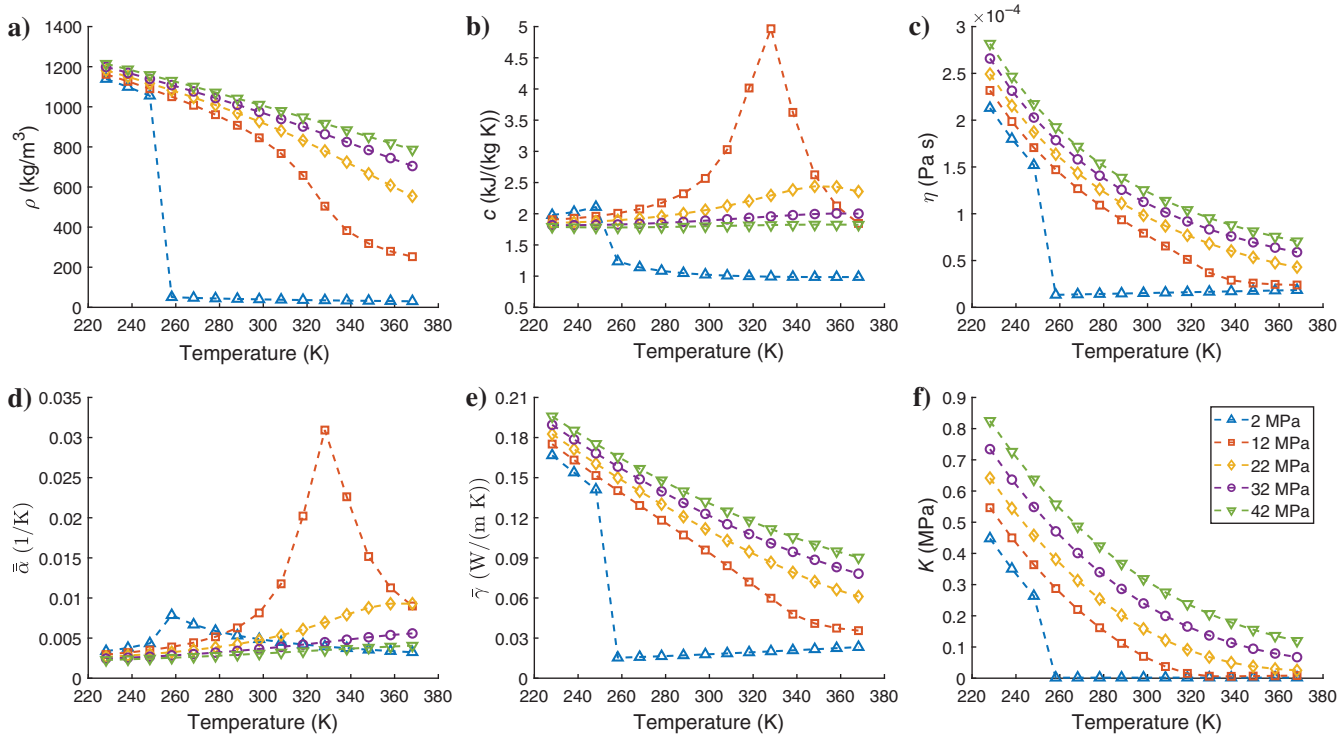

Figure 1. Temperature-dependent (a) density, (b) specific heat, (c) viscosity, (d) thermal expansion coefficient, (e) thermal conductivity, and (f) bulk modulus of CO_2 calculated by REFPROP at various pressures.

properties of the supercritical state. As shown in Figure 2e, the thermal conductivity of water is approximately 0.6–0.7 W/(m·K), more than three times that of $scCO_2$, highlighting the enhanced heat transfer facilitated by water's stronger intermolecular interactions. The bulk modulus of water exhibits a complex relationship with temperature, as shown in Figure 2f. It initially increases, then decreases with further temperature rise within the range of 280–350 K. Between 280 and 320 K, the bulk modulus increases as water molecules gain kinetic energy with rising temperature, making it more resistant to compression. However, beyond 320 K, the modulus decreases due to the weakening of hydrogen bonds and the increased disorder of water molecules as the temperature rises. A comparative analysis of water and CO_2 reveals significant disparities in their thermophysical properties, which impact injectivity, migration, and storage stability in CGS. The higher thermal conductivity and greater bulk modulus of water demonstrate superior heat transfer and sealing properties. In contrast, the lower thermal conductivity and compressibility of $scCO_2$ encounter distinct challenges in CGS.

RESULTS FOR SANDSTONE RESERVOIR

Under typical conditions for CO_2 storage, which are mostly above the critical point (Span and Wagner, 1996), the temperature ranges from 303 to 393 K, and the pressure varies between 10 and 50 MPa, corresponding to depths of 1–5 km (Awad and Espinoza, 2024). For this study, we use a sandstone reservoir at 32 MPa with a porosity of 0.2 as an example, in which phase velocity and attenuation are computed as functions of frequency and temperature, as shown in equation 13. It should be noted that the results are calculated under the condition of a constant solid skeleton temperature of 340 K, and the parameters are provided in Table 1. The temperature variations focus on the temperature-dependent properties of the pore fluid, consistent with the two-temperature assumption of the thermoporoelastic model. The relaxation time (τ_f) of water increases from 20.04 to 20.89 ns in the range of 310–340 K, whereas for CO_2, it decreases from 26.11 to 25.72 ns, where the relaxation times are calculated from the DPL heat conduction theory (Tzou, 1995; Liu et al., 2023). The thermoelastic coupling expansion coefficient ($\bar{\tilde{\alpha}}_{fs}$) varies from -0.0085 to -0.0175 K^{-1} for water and from -0.003 to -0.0033 K^{-1} for CO_2 (Singh, 2011; Lemmon et al., 2013). The coefficient of interphase heat transfer $\bar{\gamma}_{sf}$ is $1261\text{m}\cdot\text{kg}/(\text{s}^3\cdot\text{K})$ (Pecker and Deresiewicz, 1973).

Table 1. Sandstone properties.

K_s (GPa)	35
K_m (GPa)	7
μ (GPa)	5.5
ρ_s (g/cm^3)	2.65
$\mathcal{T}$	2
c_s ($\times 10^3$) (kg/(m · s^2 · K))	0.9
$\bar{\gamma}_s^*$ (m · kg/(s^3 · K))	12
$\bar{\tilde{\alpha}}_s(\times 10^{-6})$ (K^{-1})	7.2
$\bar{\kappa}$ (Darcy)	1
τ_{2s} (ns)	0.08

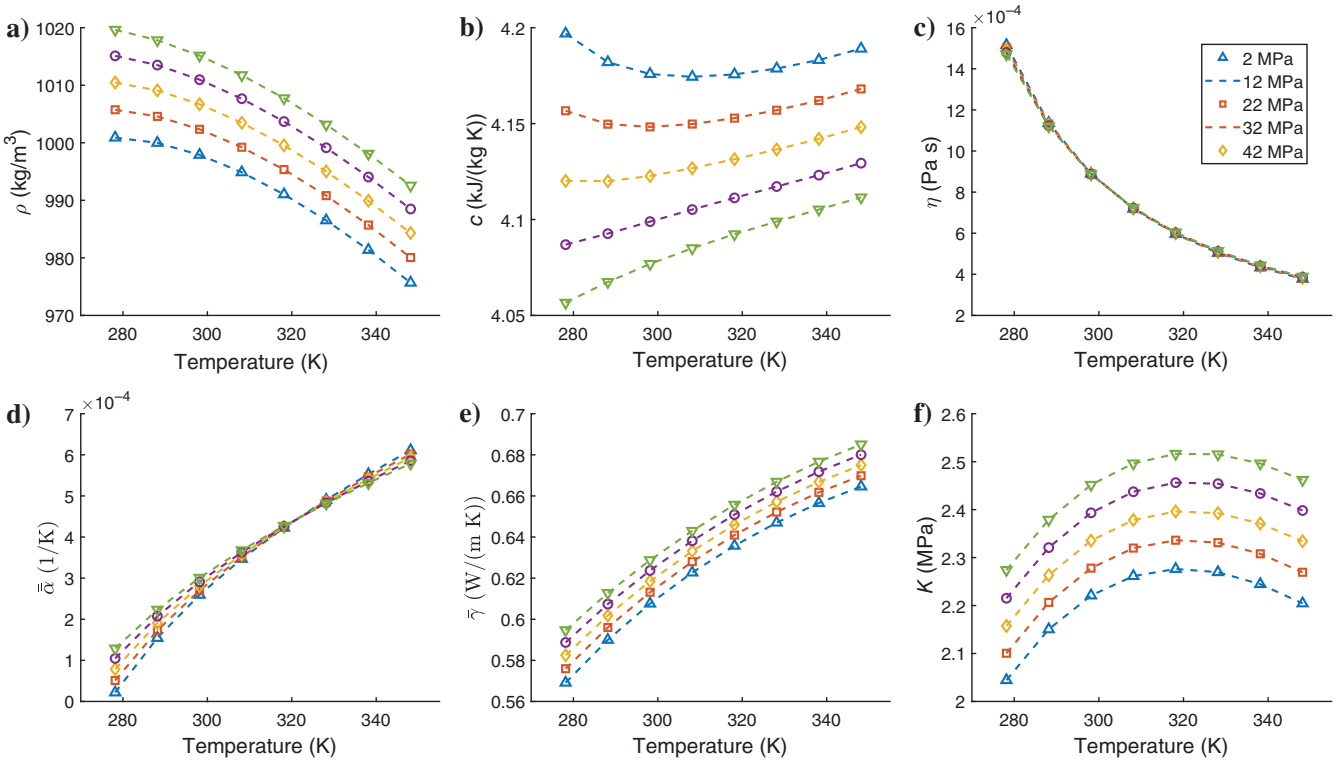

Figure 2. (a–f) The same as Figure 1a–1f, respectively, but for water.

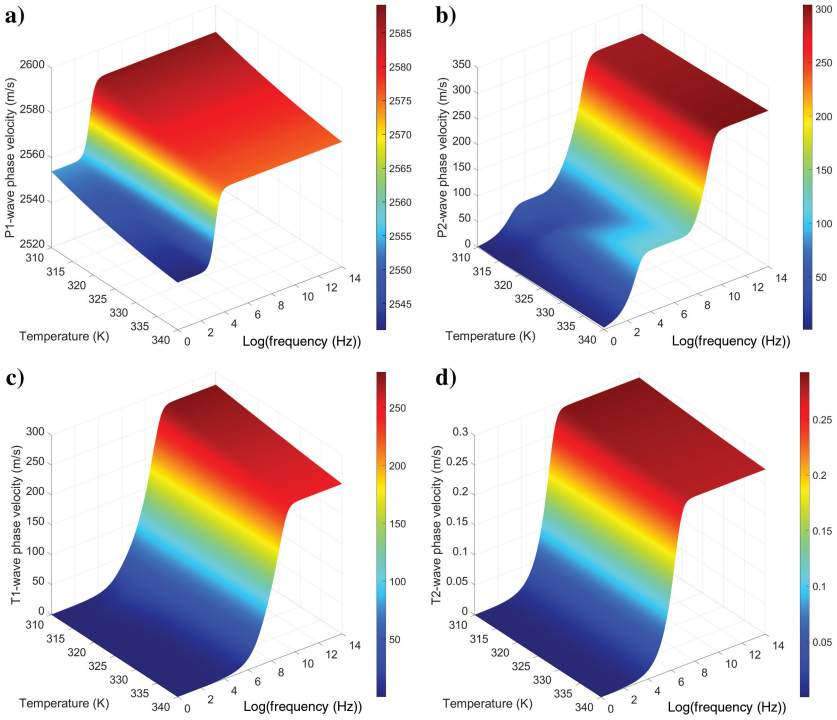

Figure 3. Phase velocities of (a) fast P (P1) wave, (b) slow P wave (P2), (c) fast T (T1) wave, and (d) slow T (T2) wave in $scCO_2$-saturated sandstone as a function of frequency and temperature.

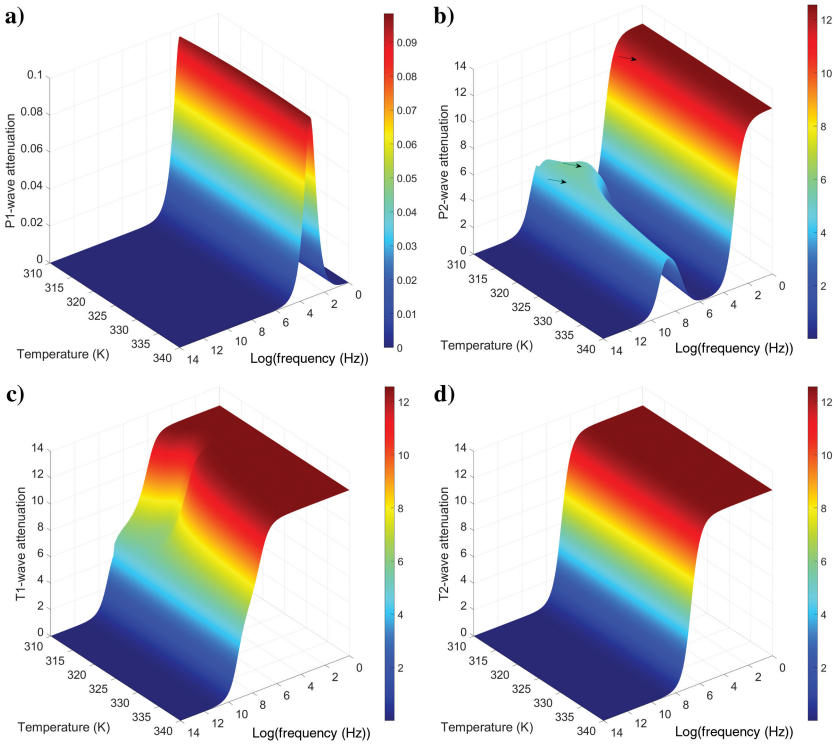

Figure 4. Attenuation coefficients of (a) fast P (P1) wave, (b) slow P wave (P2), (c) fast T (T1) wave, and (d) slow T (T2) wave in $scCO_2$-saturated sandstone as a function of frequency and temperature.

Figures 3 and 4 show the frequency- and temperature-dependent phase velocities and attenuation (calculated in equations 11 and 13) for $scCO_2$-saturated media, respectively, with the relevant fluid properties derived from Figure 1. The phase velocity of the P1 wave decreases with increasing temperature because the density of $scCO_2$ and the bulk modulus decrease due to thermal expansion. A notable inflection point is observed at approximately 1 kHz (Figure 3a), which corresponds to the Biot attenuation peak (Figure 4a) and represents the frictional energy loss caused by the filtration of pore fluids during wave excitation. As the temperature increases from 310 to 340 K, the phase velocity of the P2 wave increases by approximately 10 m/s, due to the temperature-dependent thermomechanical properties of $scCO_2$, as shown in Figure 3b. As expected, thermal effects related to the fluid have a more significant impact on the propagation of the P2 wave. Figure 4b reveals two distinct peaks and an inflection point, which correspond to inflection points in the velocity and are indicated with arrows in the figure. The first peak is associated with the Biot flow mechanism, where the fluid has sufficient time to respond to stress changes at low frequencies. As the frequency increases and approaches the thermal relaxation frequency of the solid and fluid, the second peak (at approximately 320 K) and the inflection point emerge, corresponding to thermal dispersion in the phase velocities. The T1 and P1 waves exhibit similar temperature and frequency dependencies, but they differ in their frequency dispersion properties. Specifically, the T1 wave displays dispersion and attenuation peaks at higher frequencies, as shown in Figures 3c and 4c, which are associated with thermal effects. Opposite to the P2 wave, the phase velocity of the T2 wave decreases with temperature (from 310 to 340 K), as shown in Figure 3d, likely due to the reduced thermal conductivity and increased thermal expansion coefficient of $scCO_2$ with rising temperature, which diminish the efficiency of thermal energy transfer and enhance thermally induced softening effects in the porous medium, as shown in Figure 1. The single attenuation peak observed in Figure 4d as a function of frequency is linked to the thermal effects of $scCO_2$. The sensitivities of specific heat and the thermal expansion coefficient increase with temperature (Figure 1b and 1d) at 32 MPa, which influences the effective stress within the porous medium and the propagation velocities. In contrast, the thermal conductivity of $scCO_2$ decreases with increasing temperature (Figure 1e), which is counterintuitive compared with typical gases, and influences the temperature distribution and the wave propagation characteristics.

The phase velocity of the P1 wave in water-saturated rock exhibits a distinctive temperature-dependent trend, initially increasing and then decreasing at approximately 320 K, as shown in Figure 5a. This behavior contrasts with the monotonic decrease observed for the $scCO_2$-saturated rock. The increasing velocities are attributed to the reduced viscosity of water, which enhances energy transmission. However, as hydrogen bonds weaken and water molecules become more disordered, the bulk modulus of water decreases (Figure 2f), leading to a reduction in velocities. Compared with the $scCO_2$-saturated rock, the Biot attenuation peak frequency for the water-saturated rock is higher (approximately 10 kHz in Figure 6a) due to its higher viscosity and lower compressibility. In Figures 5b and 6b, the frequency-dependent velocity and attenuation of P2 waves show a single distinct Biot peak, which differs from the behavior observed in the $scCO_2$-saturated medium. The less pronounced thermal attenuation peaks may be due to enhanced intermolecular interactions and energy transfer in water. T1 and T2 waves exhibit dispersion properties similar to those in the $scCO_2$-saturated medium, but the fluid thermal attenuation of the T1 wave is more significant. To better compare the effects of temperature on CO_2- and water-saturated sandstones, we select two different temperatures of TTG theory and the Biot case, as shown in Figure 7. In the water-saturated case of TTG, velocities reach up to 2920 m/s, compared with approximately 2570 m/s for the CO_2-saturated sandstone at 410.15 K. This discrepancy is due to the higher bulk modulus and density of water, which enhance the stiffness and energy propagation efficiency. In contrast, the Biot attenuation peak for the CO_2-saturated medium is significantly higher, reaching approximately 0.1. Compared with the Biot poroelastic model, the velocities of the TTG theory are more sensitive to temperature due to the comprehensive consideration of thermal effects.

To validate the proposed model, we compare numerical predictions with laboratory data from previous studies. Figures 8 and 9 show the model results and experimental data as a function of CO_2 saturation. Figure 8 compares model predictions with measurements by Shi et al. (2007), in which CO_2 was injected into a pure water-saturated sandstone sample at 10 MPa pore pressure and 307.15 K. Figure 9 uses data from Zhang et al. (2015), which is based on the sandstone core saturated with CO_2 and brine under 12 MPa pressure and 323.15 K. The P1-wave velocity ratio is a critical parameter in reservoir characterization, as it reflects the impact of fluid substitution on the elastic properties of the rock,

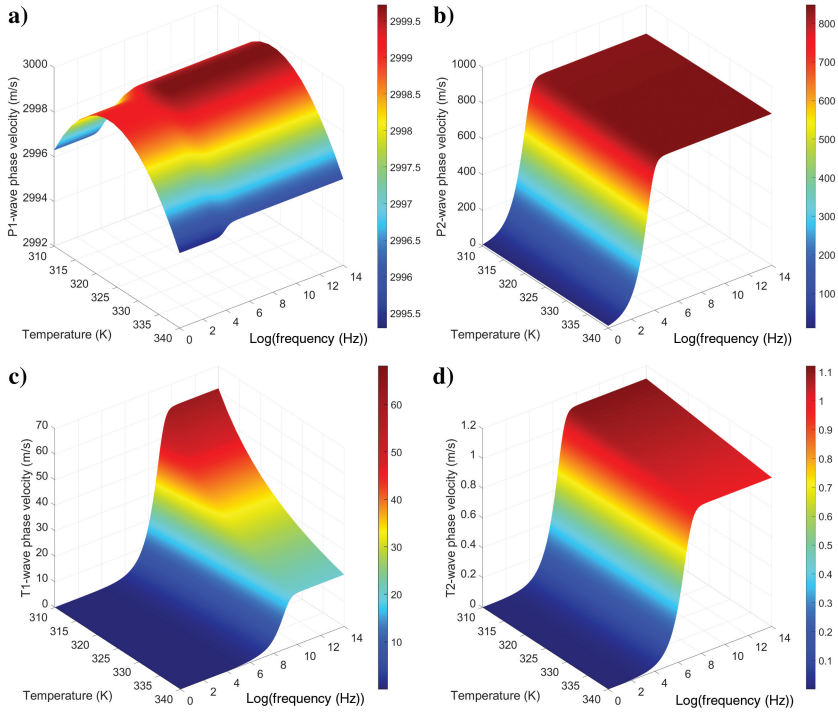

Figure 5. Phase velocities of (a) fast P (P1) wave, (b) slow P wave (P2), (c) fast T (T1) wave, and (d) slow T (T2) wave in water-saturated sandstone as a function of frequency and temperature.

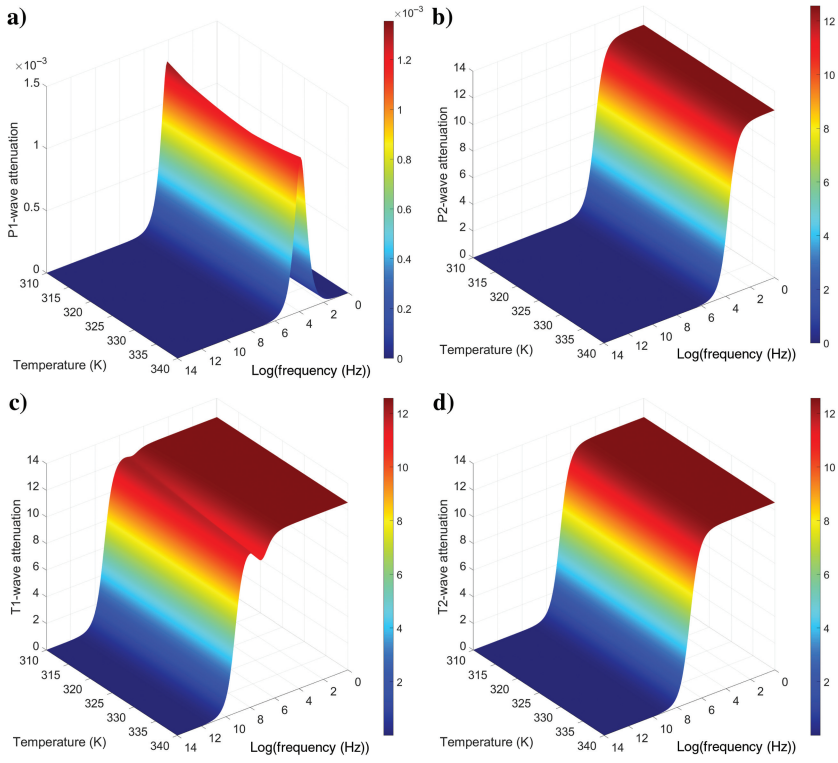

Figure 6. Attenuation coefficients of (a) fast P (P1) wave, (b) slow P wave (P2), (c) fast T (T1) wave, and (d) slow T (T2) wave in water-saturated sandstone as a function of frequency and temperature.

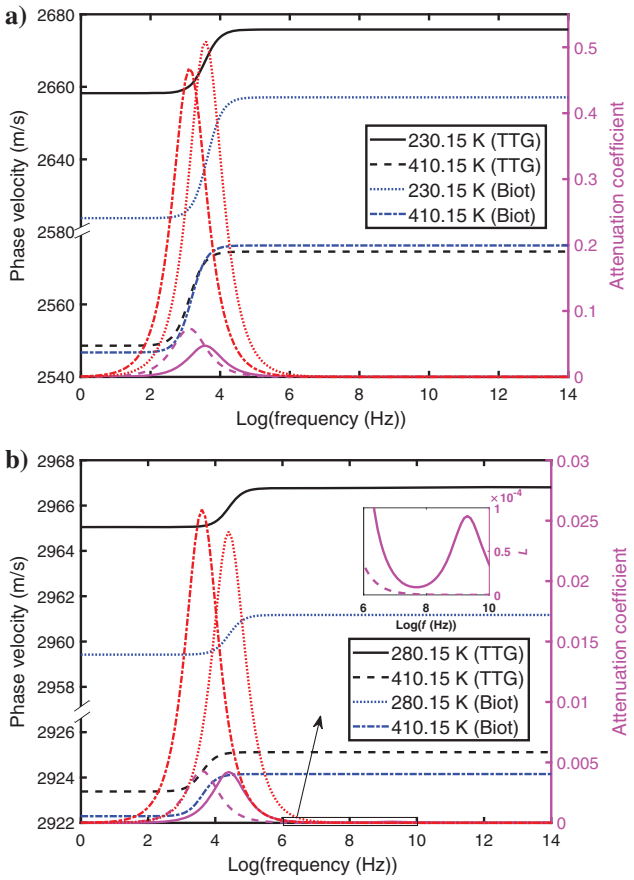

Figure 7. Phase velocities (blue and black lines) and attenuation coefficients (red and magenta lines) of the fast P wave in (a) CO_2-saturated and (b) water-saturated sandstone as a function of frequency for different temperatures, where blue lines correspond to Biot poroelastic theory.

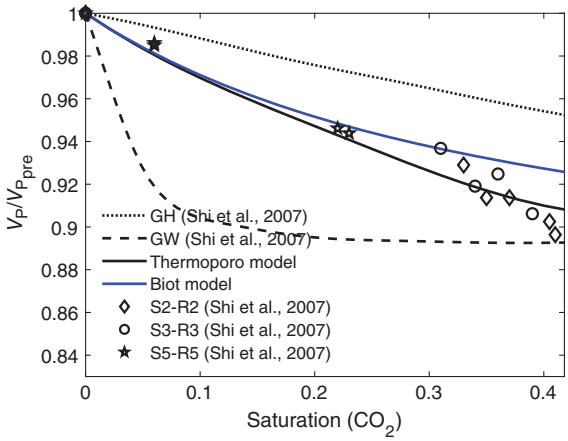

Figure 8. Predicted and measured (Shi et al., 2007) P-wave velocity ratio as a function of the $scCO_2$ saturation at 1 MHz. The Gassmann-Hill (GH) and Gassmann-Wood (GW) bounds are shown for comparison.

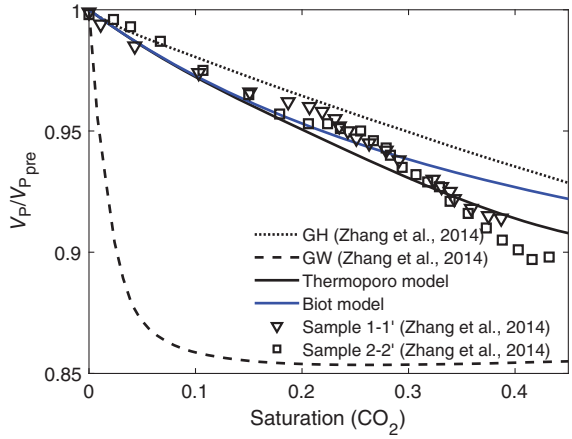

Figure 9. Predicted and measured (Zhang et al., 2015) P-wave velocity ratio as a function of the $scCO_2$ saturation at 500 KHz. The GH and GW bounds are shown for comparison.

where V_{pre} represents the velocity of water-saturated sandstone. At low $scCO_2$ saturation, the ratio is close to one, indicating that the presence of $scCO_2$ has a negligible effect. As the saturation increases, a noticeable decrease in the P1-wave velocity is observed, which is attributed to the lower density and bulk modulus of $scCO_2$ compared with water. To further evaluate the performance of the TTG model, we also compare the predictions from Biot's poroelastic isothermal theory. Although Biot's model can describe the low-saturation asymptotic behavior, it does not incorporate fluid-solid thermal interaction and thus significantly fails to reproduce the wave velocity variations observed in experiments with increasing saturation, as shown in Figures 8 and 9. Compared with the Biot theory, the experimental data show a closer agreement with the trend predicted by the TTG model proposed in this study. It should be noted that the numerical simulations assume immiscible fluid phases, consisting of pure water and $scCO_2$, which may introduce discrepancies when compared with experimental systems involving brine or partial miscibility. Additional deviation may include the rock's microstructural complexity and nonuniform pore-scale distribution of CO_2.

CONCLUSION

This study investigates the two-temperature thermoporoelastic model to explore how temperature and saturation affect seismic velocity and attenuation in sandstone reservoirs. The results demonstrate that the thermoelastic properties of CO_2 and water are significantly sensitive to pressure and temperature, leading to distinct seismic responses. In water-saturated sandstone, the P1-wave velocity exhibits an initial increase followed by a decrease, whereas, in $scCO_2$-saturated conditions, the velocity continuously declines. In addition, the Biot attenuation peak in water-saturated rocks occurs at higher frequencies compared with the $scCO_2$ case. The results emphasize the critical role of fluid properties in affecting seismic behavior and highlight the model's capability to capture the complex interactions between temperature variations and fluid substitution. Notably, the predicted P1-wave velocities show agreement with experimental data despite the inherent microstructural

complexities of the rock. In addition, the pronounced thermal attenuation observed in T waves suggests their potential as sensitive indicators for thermal variations within subsurface environments. Overall, the two-temperature thermoporoelastic model not only advances theoretical understanding of thermo-mechanical interactions in fluid-saturated sandstones but also provides a significant potential for CO_2 sequestration monitoring. This enhanced predictive capability has substantial potential for improving real-time seismic monitoring techniques, contributing to safer and more efficient geologic carbon storage.

ACKNOWLEDGMENTS

This work was supported by the National Natural Science Foundation of China under grant 42230803 and 41821002.

DATA AND MATERIALS AVAILABILITY

Data associated with this research are available and can be obtained by contacting the corresponding author.

APPENDIX A

EXPRESSIONS OF PARAMETERS IN THERMOPOROELASTIC EQUATIONS

This appendix provides explicit definitions of parameters used in the thermoporoelastic equations (equations 1–4), which are essential for accurately describing the thermal-mechanical coupling effects between solid and fluid phases. These parameters include Lamé constants (μ and λ), the bulk modulus (K), the bulk specific heat (c), thermal relaxation times (τ), thermoelasticity coefficient (β), the thermal expansion coefficients ($\bar{\tilde{\alpha}}$), and the thermal conductivity ($\bar{\gamma}^*$) (Pecker and Deresiewicz, 1973; Youssef, 2007; Carcione et al., 2019). In a linear isotropic medium, the strain (ϵ) and displacement relations are given by

$$\epsilon_m = u_{x,x} + u_{y,y} + u_{z,z}, \quad \epsilon_f = w_{x,x} + w_{y,y} + w_{z,z}, \tag{A-1}$$

and the expressions of $\wedge_{ij}$ and $\wedge^2_{ij}$ in equations 3 and 4 are

$$\begin{aligned} &\wedge_{ij} = 1 + \tau_{ij}\partial_t, \\ &\wedge^2{}_{ij} = \partial_t + \tau_{ij}\partial_{tt}, \quad \iota = 1,2,3, \quad \jmath = s,f, \end{aligned} \tag{A-2}$$

where $\tau_{1j} = 0$ and $\tau_{2j} = \tau_{3j}$ (Carcione et al., 2019) represent TTG thermoporoelastic LS theories (for the generalized case with $\tau_{2j} \neq \tau_{3j}$), in the case of the TTG-GL equation with $\tau_{3j} = 0$, whereas both models coincide if $\tau^{\mathrm{LS}}_{2j} = \tau^{\mathrm{GL}}_{1j}$ (Wang et al., 2021).

For the matrix $\bar{\mathbf{K}}$, each element appears as

$$\begin{aligned} &E_G = \lambda + \mu + \bar{\alpha}^2 M, \quad \bar{\alpha} = 1 - \frac{K_m}{K_s}, \\ &M = \left(\frac{\bar{\alpha} - \bar{\phi}}{K_s} + \frac{\bar{\phi}}{K_f}\right)^{-1}, \quad K_m = \lambda + \frac{2}{3}\mu, \\ &\beta = \beta_s + \beta_f \bar{\alpha}, \ \beta_f = 3\bar{\phi}M[(\bar{\alpha} - \bar{\phi})\bar{\tilde{\alpha}}_s + \bar{\phi}\bar{\tilde{\alpha}}_f], \\ &\beta_s = 3[(K_m + (\bar{\alpha} - \bar{\phi})^2 M)\bar{\tilde{\alpha}}_s + \bar{\phi}(\bar{\alpha} - \bar{\phi})M\bar{\tilde{\alpha}}_f], \\ &R_{11} = (1 - \bar{\phi})\beta_s, \quad R_{22} = 3M\bar{\phi}\bar{\tilde{\alpha}}_f, \quad R_{12} = \bar{\alpha}\beta_f, \\ &R_{21} = 3M(\bar{\alpha} - \bar{\phi})(1 - \bar{\phi})\bar{\tilde{\alpha}}_s, \quad F_{11} = (1 - \bar{\phi})c_s\rho_s, \\ &F_{22} = \bar{\phi}c_f\rho_f, \quad F_{12} = -3\bar{\tilde{\alpha}}_s R_{12} T_0^s + \bar{\tilde{\alpha}}_{fs} R_{22} T_0^f, \\ &F_{21} = -3\bar{\tilde{\alpha}}_{sf} R_{11} T_0^s + \bar{\tilde{\alpha}}_f R_{21} T_0^f, \\ &\bar{\gamma}_s = (1 - \bar{\phi})\bar{\gamma}_s^*, \quad \bar{\gamma}_f = \bar{\phi}\bar{\gamma}_f^*, \end{aligned} \tag{A-3}$$

where coefficients such as R and F represent the coupling effects between mechanical deformation and temperature fields based on TTG theory (Youssef, 2007).

APPENDIX B

THE EXPRESSIONS OF COEFFICIENTS *B*

This appendix summarizes the detailed coefficients B used in the dispersion relation of P waves (equation 11):

$$\begin{aligned} &B_8 = EM\bar{\gamma}_s\bar{\gamma}_f, \\ &B_6 = \omega\{-a_{61}\bar{\gamma}_s\bar{\gamma}_f - EMa_{62} + \mathrm{i}[E_G a_{64} T_0^f + M(a_{65} + a_{66})]\} \\ &\quad + EM\bar{\gamma}_{sf}(\bar{\gamma}_s + \bar{\gamma}_f), \\ &B_4 = \mathrm{i}\omega\bar{\gamma}_{sf}(T_0^f a_{41} - T_0^s M a_{42}) - \omega^2 T_0^s T_0^f a_{44} \\ &\quad + \mathrm{i}\omega^2(a_{45} + a_{46} + a_{47} + a_{48}) - \omega a_{49}, \\ &B_2 = \mathrm{i}\omega^3(a_{26} + a_{27}) - \mathrm{i}\omega^2 a_{28} + a_{29}, \\ &B_0 = \omega^4 a_{43}(\omega\bar{\tau}_{f2}\bar{\tau}_{s2}a_{63} + \bar{\gamma}_{sf}a_{25}), \end{aligned} \tag{B-1}$$

where

$$E = \lambda + 2\mu, \ \bar{\tau}_{\iota j} = \mathrm{i} + \omega\tau_{\iota j}, \tag{B-2}$$

where $\iota = 1,2,3$ and $j = s,f$. The coefficients a are

$$\begin{aligned} a_{61} &= -\omega M(2\bar{\alpha}\rho_f - \rho) + E_G(\mathrm{i}b + m\omega), \\ a_{62} &= F_{11}\bar{\tau}_{s2}\bar{\gamma}_f + F_{22}\bar{\gamma}_s\bar{\tau}_{f2}, \\ a_{63} &= F_{12}F_{21} - F_{11}F_{22}, \\ a_{64} &= R_{21}^2\bar{\gamma}_f\bar{\tau}_{s1}\bar{\tau}_{s3} + R_{22}^2\bar{\gamma}_s\bar{\tau}_{f1}\bar{\tau}_{f3}, \\ a_{65} &= R_{11}\bar{\gamma}_f\bar{\tau}_{s1}\bar{\tau}_{s3}[R_{11}T_0^s - \bar{\alpha}R_{21}(T_0^s + T_0^f)], \\ a_{66} &= R_{12}\bar{\gamma}_s\bar{\tau}_{f1}\bar{\tau}_{f3}[R_{12}T_0^s - \bar{\alpha}R_{22}(T_0^s + T_0^f)], \end{aligned} \tag{B-3}$$

$$
\begin{aligned}
a_{41} &= (R_{21}\bar{\tau}_{s3} + R_{22}\bar{\tau}_{f3})[E_G(R_{21}\bar{\tau}_{s1} + R_{22}\bar{\tau}_{f1}) \\
&- M\bar{\alpha}(R_{11}\bar{\tau}_{s1} + R_{12}\bar{\tau}_{f1})], \\
a_{42} &= (R_{11}\bar{\tau}_{s3} + R_{12}\bar{\tau}_{f3})[\bar{\tau}_{f1}(\bar{\alpha}R_{22} - R_{12}) + \bar{\tau}_{s1}(\bar{\alpha}R_{21} - R_{11})], \\
a_{43} &= \omega\rho_f^2 - (m\omega + \mathrm{i}b)\rho, \\
a_{44} &= \bar{\tau}_{f1}\bar{\tau}_{f3}\bar{\tau}_{s1}\bar{\tau}_{s3}(R_{11}R_{22} - R_{12}R_{21})^2, \\
a_{45} &= \bar{\tau}_{f1}\bar{\tau}_{f3}\{T_0^f R_{22}^2(-E_G\bar{\tau}_{s2}F_{11} - \omega\rho\bar{\gamma}_s) \\
&+ R_{22}R_{12}(T_0^s + T_0^f)(M\bar{\alpha}F_{11}\tau_{s2} + \omega\bar{\gamma}_s\rho_f) \\
&- R_{12}^2 T_0^s[MF_{11}\bar{\tau}_{s2} + \bar{\gamma}_s(m\omega + \mathrm{i}b)]\}, \\
a_{46} &= \bar{\tau}_{s1}\bar{\tau}_{s3}\{T_0^f R_{21}^2(-E_G\bar{\tau}_{f2}F_{22} - \omega\rho\bar{\gamma}_f) \\
&+ R_{21}R_{11}(T_0^s + T_0^f)(M\bar{\alpha}F_{22}\tau_{f2} + \omega\bar{\gamma}_f\rho_f) \\
&- R_{11}^2 T_0^s[MF_{22}\bar{\tau}_{f2} + \bar{\gamma}_f(m\omega + \mathrm{i}b)]\}, \\
a_{47} &= \bar{\tau}_{s3}\bar{\tau}_{f1}\bar{\tau}_{f2}F_{21}[R_{11}T_0^s M(R_{12} - \bar{\alpha}R_{22}) \\
&+ R_{21}T_0^f(R_{22}E_G - \bar{\alpha}MR_{12})], \\
a_{48} &= \bar{\tau}_{f3}\bar{\tau}_{s1}\bar{\tau}_{s2}F_{12}[R_{12}T_0^s M(R_{11} - \bar{\alpha}R_{21}) \\
&+ R_{22}T_0^f(R_{21}E_G - \bar{\alpha}MR_{11})], \\
a_{49} &= \omega^2 a_{43}\bar{\gamma}_s\bar{\gamma}_f + \omega(EMa_{63}\bar{\tau}_{s2}\bar{\tau}_{f2} - a_{61}a_{62}) \\
&+ \bar{\gamma}_{sf}(a_{61}(\bar{\gamma}_s + \bar{\gamma}_f) + EMa_{25}),
\end{aligned}
\tag{B-4}
$$

$$
\begin{aligned}
&a_{21} = \omega T_0^f(R_{21}\rho - R_{11}\rho_f),\ a_{22} = T_0^s[R_{11}(m\omega + \mathrm{i}b) - \omega\rho_f R_{21}], \\
&a_{23} = \omega T_0^f(R_{12}\rho_f - R_{22}\rho),\ a_{24} = T_0^s[-R_{12}(m\omega + \mathrm{i}b) + \omega\rho_f R_{22}], \\
&a_{25} = \bar{\tau}_{s2}(F_{11} + F_{12}) + \bar{\tau}_{f2}(F_{21} + F_{22}), \\
&a_{26} = \bar{\tau}_{f2}\bar{\tau}_{s3}[F_{22}\bar{\tau}_{s1}(a_{21}R_{21} + a_{22}R_{11}) \\
&+ F_{21}\bar{\tau}_{f1}(a_{23}R_{21} + a_{24}R_{11})], \\
&a_{27} = -\bar{\tau}_{f3}\bar{\tau}_{s2}[F_{12}\bar{\tau}_{s1}(a_{21}R_{22} + a_{22}R_{12}) \\
&+ F_{11}\bar{\tau}_{f1}(a_{23}R_{22} + a_{24}R_{12})], \\
&a_{28} = \bar{\gamma}_{sf}[(R_{21}\bar{\tau}_{s3} + R_{22}\bar{\tau}_{f3})(a_{21}\bar{\tau}_{s1} - a_{23}\bar{\tau}_{f1}) \\
&+ (R_{11}\bar{\tau}_{s3} + R_{12}\bar{\tau}_{f3})(a_{22}\bar{\tau}_{s1} - a_{24}\bar{\tau}_{f1})], \\
&a_{29} = \omega^2[a_{43}a_{62}\omega^2 + a_{25}a_{61}\bar{\gamma}_{sf} \\
&+ \omega(a_{61}a_{63}\bar{\tau}_{s2}\bar{\tau}_{f2} - a_{43}\bar{\gamma}_{sf}(\bar{\gamma}_s + \bar{\gamma}_f))].
\end{aligned}
\tag{B-5}
$$

REFERENCES

Aminu, M. D., S. A. Nabavi, C. A. Rochelle, and V. Manovic, 2017, A review of developments in carbon dioxide storage: Applied Energy, **208**, 1389–1419, doi: 10.1016/j.apenergy.2017.09.015.

Awad, M. M., and D. N. Espinoza, 2024, Mudrock wettability at pressure and temperature conditions for CO2 geological storage: International Journal of Greenhouse Gas Control, **135**, 104160, doi: 10.1016/j.ijggc.2024.104160.

Biot, M. A., 1956, Theory of elastic waves in fluid-saturated porous solid. I. Low frequency range: Journal of the Acoustical Society of America, **28**, 168–178, doi: 10.1121/1.1908239.

Biot, M. A., 1962, Mechanics of deformation and acoustic propagation in porous media: Journal of Applied Physics, **33**, 1482–1498, doi: 10.1063/1.1728759.

Carcione, J. M., F. Cavallini, E. Wang, J. Ba, and L. Y. Fu, 2019, Physics and simulation of wave propagation in linear thermoporoelastic media: Journal of Geophysical Research: Solid Earth, **124**, 124–145, doi: 10.1029/2019JB017851.

Carcione, J. M., Z. W. Wang, W. Ling, E. Salusti, J. Ba, and L. Y. Fu, 2018, Simulation of wave propagation in linear thermoelastic media: Geophysics, **84**, no. 1, T1–T11, doi: 10.1190/geo2018-0448.1.

Creasy, N., L. Huang, E. Gasperikova, W. Harbert, T. Bratton, and Q. Zhou, 2024, CO2 rock physics modeling for reliable monitoring of geologic carbon storage: Communications Earth & Environment, **5**, 333, doi: 10.1038/s43247-024-01493-6.

Deng, W., L. Y. Fu, I. B. Morozov, and Z. Wang, 2024, Macroscopic mechanical properties of fluid-saturated sandstone at variable temperatures: Geophysics, **88**, no. 3, MR127–MR139, doi: 10.1190/geo2022-0427.1.

Dowell, N. M., N. Florin, A. Buchard, J. Hallett, A. Galindo, G. Jackson, C. S. Adjiman, C. K. Williams, N. Shah, and P. Fennell, 2010, An overview of CO2 capture technologies: Energy & Environmental Science, **3**, 1645–1669, doi: 10.1039/C004106H.

Fentaw, J. W., H. Emadi, A. Hussain, D. M. Fernandez, and S. R. Thiyagarajan, 2024, Geochemistry in geological CO2 sequestration: A comprehensive review: Energies, **17**, 5000, doi: 10.3390/en17195000.

Green, A. E., and K. A. Lindsay, 1972, Thermoelasticity: Journal of Elasticity, **2**, 1–7, doi: 10.1007/BF00045689.

Hou, W., L. Y. Fu, and J. M. Carcione, 2023, Amplitude-variation-with-offset in thermoelastic media: Geophysics, **88**, no. 1, MR25–MR33, doi: 10.1190/geo2021-0815.1.

Hou, W., L. Y. Fu, and J. M. Carcione, 2024, Reflection, transmission, and AVO response of inhomogeneous plane waves in thermoporoelastic media with two-temperature equations of heat conduction: Geophysics, **89**, no. 5, MR297–MR307, doi: 10.1190/geo2023-0625.1.

Hou, W., L. Y. Fu, J. M. Carcione, Z. Wang, and J. Wei, 2021, Simulation of thermoelastic waves based on the Lord-Shulman theory: Geophysics, **86**, no. 3, T155–T164, doi: 10.1190/geo2020-0515.1.

Kalam, S., T. Olayiwola, M. M. Al-Rubaii, B. I. Amaechi, M. S. Jamal, and A. A. Awotunde, 2021, Carbon dioxide sequestration in underground formations: Review of experimental, modeling, and field studies: Journal of Petroleum Exploration and Production, **11**, 303–325, doi: 10.1007/s13202-020-01028-7.

Lebedev, M., O. Bilenko, V. Mikhaltsevitch, M. Pervukhina, and B. Gurevich, 2014, Laboratory measurements of ultrasonic velocities in CO2 saturated brines: Energy Procedia, **63**, 4273–4280, doi: 10.1016/j.egypro.2014.11.462.

Lemmon, E. W., M. L. Huber, and M. O. McLinden, 2013, NIST standard reference database 23. Reference fluid thermodynamic and transport properties (REFPROP), version, 9.1: National Institute of Standards and Technology.

Li, N., W. Deng, L. Y. Fu, J. M. Carcione, and T. Han, 2024, Wave propagation in double-porosity thermoelastic media: Geophysics, **87**, no. 6, MR265–MR277, doi: 10.1190/geo2022-0008.1.

Li, N., L. Y. Fu, W. Deng, J. M. Carcione, and J. Yang, 2023, A thermo-hydro-mechanical model to evaluate the seismic properties of geothermal reservoirs: Geophysics, **88**, no. 5, WB23–WB35, doi: 10.1190/geo2022-0491.1.

Liao, G., Y. Du, F. Zhang, and J. Q. E, 2023, Comprehensive review on physical properties of supercritical carbon dioxide calculated by molecular simulation: Korean Journal of Chemical Engineering, **40**, 11–36, doi: 10.1007/s11814-022-1316-8.

Lin, Z., Y. Kuang, W. Li, and Y. Zheng, 2024, Research status and prospects of CO2 geological sequestration technology from onshore to offshore: A review: Earth-Science Reviews, **258**, 104928, doi: 10.1016/j.earscirev.2024.104928.

Liu, Y., L. Y. Fu, W. Deng, W. Hou, J. M. Carcione, and J. Wei, 2023, Simulation of wave propagation in thermoporoelastic media with dual-phase-lag heat conduction: Journal of Thermal Stresses, **46**, 620–638, doi: 10.1080/01495739.2023.2193225.

Lord, N. E., and Y. Shulman, 1967, A generalized thermomechanical theory of elastic media: Journal of Mathematical Physics, **8**, 1951–1961.

Noda, N., 1990, Thermal stress problem in a fluid-filled porous circular cylinder: Zeitschrift fur Angewandte Mathematik und Mechanik, **70**, 543–549, doi: 10.1002/zamm.19900701203.

Otu, S., A. J. Rinehart, A. J. Luhmann, J. Simmons, and P. Mozley, 2023, Effects of CO2 on creep deformation in sandstones at carbon sequestration reservoir conditions: An experimental study: International Journal of Greenhouse Gas Control, **129**, 103970, doi: 10.1016/j.ijggc.2023.103970.

Parisio, F., and V. Vilarrasa, 2020, Sinking CO2 in supercritical reservoirs: Geophysical Research Letters, **47**, e2020GL090456, doi: 10.1029/2020GL090456.

Pecker, C., and H. Deresiewicz, 1973, Thermal effects on wave propagation in liquid-filled porous media: Acta Mechanica, **16**, 45–64, doi: 10.1007/BF01177125.

Shi, J. Q., and S. Durucan, 2005, CO2 storage in deep unminable coal seams: Oil & Gas Science and Technology, **60**, 547–558, doi: 10.2516/ogst:2005037.

Shi, J. Q., Z. Xue, and S. Durucan, 2007, Seismic monitoring and modelling of supercritical CO2 injection into a water-saturated sandstone: Interpretation of P-wave velocity data: International Journal of Greenhouse Gas Control, **1**, 473–480, doi: 10.1016/S1750-5836(07)00013-8.

Singh, B., 2011, On propagation of plane waves in generalized porothermoelasticity: Bulletin of the Seismological Society of America, **101**, 756–762, doi: 10.1785/0120100091.

Span, R., and W. Wagner, 1996, A new equation of state for carbon dioxide covering the fluid region from the triple-point temperature to 1100 K at pressures up to 800 MPa: Journal of Physical and Chemical Reference Data, **25**, 1509–1596, doi: 10.1063/1.555991.

Tzou, D. Y., 1995, A unified field approach for heat conduction from macro- to micro-scales: ASME Journal of Heat Transfer, **117**, 8–16, doi: 10.1115/1.2822329.

Wang, E., J. M. Carcione, Y. Yuan, and J. Ba, 2021, Reflection of inhomogeneous plane waves at the surface of a thermo-poroelastic medium: Geophysical Journal International, **224**, 1621–1639, doi: 10.1093/gji/ggaa543.

Wang, Z., L. Y. Fu, J. M. Carcione, W. Hou, and J. Wei, 2022, Analytical solution of thermoelastic attenuation in fine layering for random variations of the Grüneisen ratio: Journal of Thermal Stresses, **45**, 630–640, doi: 10.1080/01495739.2022.2074930.

Wei, J., L. Y. Fu, J. M. Carcione, and W. Deng, 2023, An elastic dispersion and attenuation of P-and SV-wave scattering by aligned non-isothermal inclusions of finite thickness: Geophysics, **88**, no. 3, MR95–MR104, doi: 10.1190/geo2022-0321.1.

Wei, J., L. Y. Fu, J. M. Carcione, and T. Han, 2022, Wave-induced thermal flux and scattering of P waves in a medium with aligned circular cracks: Geophysics, **87**, no. 5, MR209–MR218, doi: 10.1190/geo2021-0616.1.

Wei, J., L. Y. Fu, T. Han, and J. M. Carcione, 2020, Thermoelastic dispersion and attenuation of P and SV wave scattering by aligned fluid-saturated cracks of finite thickness in an isothermal elastic medium: Journal of Geophysical Research: Solid Earth, **125**, e2020JB019942, doi: 10.1029/2020JB019942.

Xi, D., X. Liu, and C. Zhang, 2007, The frequency (or time)-temperature equivalence of relaxation in saturated rocks: Pure and Applied Geophysics, **164**, 2157–2173, doi: 10.1007/s00024-007-0270-z.

Xi, D., S. Xu, Y. Du, and L. Yi, 2011, Wave propagation analysis of porous rocks with the thermal activated relaxation mechanism: Journal of Applied Geophysics, **73**, 289–303, doi: 10.1016/j.jappgeo.2011.01.013.

Xue, Z., and X. Lei, 2006, Laboratory study of CO2 migration in water-saturated anisotropic sandstone, based on P-wave velocity imaging: Exploration Geophysics, **37**, 10–18, doi: 10.1071/EG06010.

Youssef, H. M., 2007, Theory of generalized porothermoelasticity: International Journal of Rock Mechanics and Mining Sciences, **44**, 222–227, doi: 10.1016/j.ijrmms.2006.07.001.

Zhang, C., H. Zhang, R. Song, Z. Wang, G. Jiang, Y. Zuo, J. Hu, and R. Huang, 2024, Simulation of thermo-hydro-mechanical coupled heat extraction process of geothermal reservoir under varied geological conditions with CO2 as working fluid: Journal of Hydrology, **629**, 130549, doi: 10.1016/j.jhydrol.2023.130549.

Zhang, Y., O. Nishizawa, T. Kiyama, and Z. Xue, 2015, Saturation-path dependency of P-wave velocity and attenuation in sandstone saturated with CO2 and brine revealed by simultaneous measurements of waveforms and X-ray computed tomography images: Geophysics, **80**, no. 4, D403–D415, doi: 10.1190/geo2014-0289.1.

Zimmerman, R. W., 2000, Coupling in poroelasticity and thermoelasticity: International Journal of Rock Mechanics and Mining Sciences, **37**, 79–87, doi: 10.1016/S1365-1609(99)00094-5.

Biographies and photographs of the authors are not available.